



# Charge-ordered Cu<sup>+</sup>/Cu<sup>2+</sup> pair regulated highly-selective electroreduction of carbon monoxide to acetate



Siyuan Luo <sup>a,1</sup>, Haiyuan Zou <sup>b,1</sup>, Renji Zheng <sup>a,c,1</sup>, Shimao Deng <sup>a,d,1</sup>, Xuezhen Feng <sup>a</sup>, Wenfei Wei <sup>a</sup>, Ranhao Wang <sup>a</sup>, Ze Li <sup>e</sup>, Wei Xu <sup>e</sup>, Lele Duan <sup>b,2</sup>, Hong Chen <sup>a,\*,2</sup>

<sup>a</sup> State Environmental Protection Key Laboratory of Integrated Surface Water Groundwater Pollution Control, Guangdong Provincial Key Laboratory of Soil and Groundwater Pollution Control, Key Laboratory of Municipal Solid Waste Recycling Technology and Management of Shenzhen City, Shenzhen Key Laboratory of Interfacial Science and Engineering of Materials (SKLISEM), School of Environmental Science and Engineering, Southern University of Science and Technology, Shenzhen, 518055, China

<sup>b</sup> Department of Chemistry, Southern University of Science and Technology, Shenzhen, 518055, China

<sup>c</sup> School of Minerals Processing and Bioengineering, Central South University, Changsha, 410083, China

<sup>d</sup> Eastern Institute for Advanced Study, Eastern Institute of Technology, Ningbo, China

<sup>e</sup> Beijing National Laboratory for Molecular Sciences, Key Laboratory of Organic Solids, Institute of Chemistry, Chinese Academy of Sciences, Beijing, 100190, China

## ARTICLE INFO

### Keywords:

CO electroreduction  
Selective reduction  
Charge order  
Electronic structure regulation

## ABSTRACT

Selective electrochemical reduction of CO<sub>2</sub>/CO to high-valuable C<sub>2+</sub> products is of great importance to alleviate the global warming and energy crisis problems, while the selective production of C<sub>2</sub> is severely limited by the C—C coupling pathway on the catalyst interface. Herein, by employing a Cu<sup>+</sup>/Cu<sup>2+</sup> charge-ordered metal-organic framework (MOF) material (denoted to be Cu4BHT) as a CO electroreduction catalyst, a high acetate selectivity of 50.3% at  $-0.7$  V versus reversible hydrogen electrode (RHE) has been achieved. An in-depth mechanism study reveals that the charge-ordered Cu<sup>+</sup>/Cu<sup>2+</sup> pair on Cu4BHT interface favors the C=O bond activation, C—C coupling, and proton-coupled electron transfer dynamics, which results in the selective formation of C<sub>2+</sub> products. This work illustrates the critical role of employing charge-ordered Cu<sup>+</sup>/Cu<sup>2+</sup> catalytic site pair for C—C coupling, which paves the way for designing highly selective catalysts to promote the formation of the C<sub>2</sub> products.

## 1. Introduction

To alleviate global warming and the energy crisis, developing highly efficient electrocatalysts to artificially convert CO<sub>2</sub>/CO to C<sub>2</sub> products is vital and has attracted intensive attention [1]. From the reaction dynamics point of view, the C—C coupling step is considered as the most challenging and rate-determining step for obtaining C<sub>2</sub> products during the electrocatalysis process [2,3]. Benefited from the proper chemisorption affinity of active copper center towards CO<sub>2</sub>/CO adsorption for \*CO formation and subsequent C—C coupling [4–8], tremendous reported catalysts on catalytic C<sub>2+</sub> products formation have employed copper as the active catalytic sites, but byproducts, like H<sub>2</sub>, CO, CH<sub>4</sub>, and HCOOH, are inevitably generated [5,6].

Various strategies are engaged in catalyst design to facilitate the

catalytic activity and selectivity towards C<sub>2+</sub> products, including morphology engineering [9,10], heterostructure engineering [11–13], coordination engineering [14], and electronic structure regulation [15–19]. Among all these approaches, electronic structure regulation, which manipulates the intrinsic adsorption affinity of active sites towards CO<sub>2</sub>/CO, and subsequently regulates the energy barrier of C—C coupling, has been recognized as the most promising strategy. Conventional routines frequently used to regulate the electronic structure of a catalyst include element doping [15], defect engineering [16,17], and electrochemical interface reconstruction [18,19]. Although these approaches can improve the catalytic performance, the resulting active sites within catalysts are disorderly distributed, lacking spatial long-range order and homogeneity. Furthermore, the catalysts engineered via these approaches are with metastable active sites and easily

\* Corresponding author.

E-mail address: [chenh3@sustech.edu.cn](mailto:chenh3@sustech.edu.cn) (H. Chen).

<sup>1</sup> These authors contributed equally: Siyuan Luo, Haiyuan Zou, Renji Zheng and Shimao Deng.

<sup>2</sup> These authors jointly supervised this work

become deactivated under the long-term electrolysis [20–23]. Therefore, developing a novel strategy to modulate the electronic structure of electroactive sites of electrocatalysts, with well-defined long-range order and long-term stability, is crucial for achieving highly selective C–C coupling.

Charge order is defined as the electron density modulation on the same element that results in breaking lattice translational symmetry. It induces periodic lattice displacements (PLDs) via electron–lattice coupling, in which the charge is disproportionated and localized on neighboring metal sites [24]. The charge-ordering behavior of the aliovalent metal cations can periodically regulate the charge density distribution of the active metal sites over the whole catalyst and maintain the crystalline structure. In the charge-ordered solid, one metal with two valence states and charge densities arranges alternately and periodically in the crystal structure. The asymmetric charge distribution inducing electrostatic interaction between the two adjacent aliovalent metals can improve adsorption affinity towards  $\text{CO}_2/\text{CO}$  and lowering the dipole-dipole repulsion between  $^*\text{CO}$  intermediate [25], thus boosting  $\text{CO}_2/\text{CO}$  activation and C–C coupling, which may facilitate the formation of the  $\text{C}_{2+}$  products (Fig. 1).

Herein, inspired by the good adsorption affinity of copper center towards  $\text{CO}_2/\text{CO}$ , together with the charge-ordered metal pair favored on the electronic structure regulation behavior, we employed a charge-ordered Cu-based metal-organic framework (MOF; denoted as Cu4BHT), as a model electrocatalyst for electrocatalytic CO reduction (COR). Cu4BHT presents a favorable  $\text{C}_2$  production in COR and displays an optimal faradic efficiency of 68% at  $-0.8$  V versus RHE, which exceeds by a factor of 10 than a non-charge-ordered Cu-based MOF (denoted as Cu3BHT). Moreover, high acetate selectivity of 50.3% (liquid products selectivity up to 95%) has been achieved by the Cu4BHT at  $-0.7$  V versus RHE, keeping pace with top acetate selectivity in the case of CO electroreduction [26,27]. Theoretical study reveals that charge-ordered  $\text{Cu}^+/\text{Cu}^{2+}$  pair modulates the electron density distribution between two Cu atoms, facilitating the CO adsorption, activation, and C–C coupling process. The present study proposes an intriguing charge-order structural strategy for boosting the selectivity of electrocatalytic reduction of CO towards  $\text{C}_{2+}$  products, which inspires rational catalyst

designs towards high-valuable product formation.

## 2. Experimental section

### 2.1. Catalysis synthesis

#### 2.1.1. Chemical reagents

All the commercial chemicals, Tetrakis(acetonitrile)copper(I) tetrafluoroborate ( $[\text{Cu}(\text{CH}_3\text{CN})_4]\text{BF}_4$ , Bide Pharmatech Ltd., 98%), Copper (II) acetate monohydrate ( $\text{Cu}(\text{CH}_3\text{COO})_2 \cdot \text{H}_2\text{O}$ , Aladdin, 98%), Copper (II) nitrate trihydrate (Aladdin, 98%), Methanol ( $\text{CH}_3\text{OH}$ , Macklin, AR), Chloroform ( $\text{CHCl}_3$ , Aladdin, AR), Acetonitrile ( $\text{CH}_3\text{CN}$ , Aladdin, AR), Dimethylformamide (DMF, Aladdin, AR), Ethanol ( $\text{C}_2\text{H}_5\text{OH}$ , Aladdin, AR), Diethyl ether ( $\text{C}_4\text{H}_8\text{O}$ , Aladdin, AR) were used without further purification. Benzenehexathiol (BHT) was prepared according to the literature [28]. Cu3BHT [29] and Cu4BHT [30] were synthesized following the literature methods with some modifications.

#### 2.1.2. Synthesis of Cu3BHT

Cu3BHT was prepared via an interface reaction using Copper(II) nitrate and benzenehexathiol (BHT) as raw materials. Under an argon atmosphere using Schlenk line, 75 mg of BHT was dissolved in 250 mL degassed chloroform. Then the BHT chloroform solution was transferred into a 500 mL flask and kept at a temperature of 45 °C in the oil bath. Degassed water with the same temperature (200 mL) was slowly added to this solution to form an oil-water interface. 10 mL aqueous solution of 200 mg  $\text{Cu}(\text{NO}_3)_2 \cdot 3 \text{H}_2\text{O}$  was then added into the water gently using a syringe. The dark blue film can be observed at the chloroform-water interface. Leave the flask to stand for 24 hours at 45 °C, and then the solution was gently removed through a syringe; the insoluble film was washed with pure solvents in order of water, dimethylformamide, ethanol, and diethyl ether in sequent, and finally dried in vacuum at 40 °C overnight. The yield of Cu3BHT: (46 mg, Yield 30.3%).

#### 2.1.3. Synthesis of Cu4BHT

$[\text{Cu}(\text{CH}_3\text{CN})_4]\text{BF}_4$  (0.5 mM) and  $\text{Cu}(\text{CH}_3\text{COO})_2 \cdot \text{H}_2\text{O}$  (0.5 mM) were mixed and dissolved in 10 mL of methanol in a Schlenk flask under an

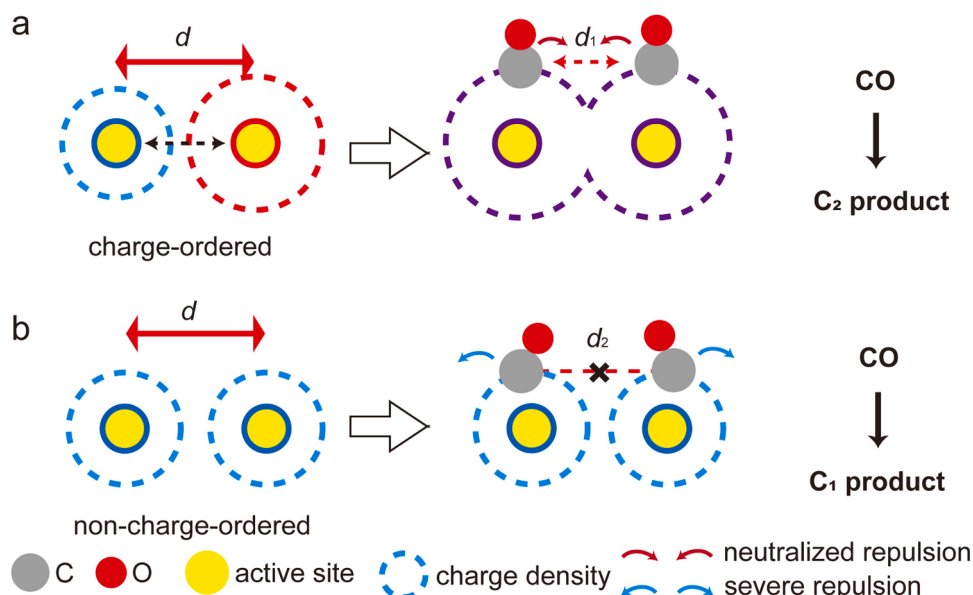


**Fig. 1.** Diagram of charge-ordered site pair for COR. a Over a charge-ordered dual-site catalyst, the electrostatic interaction induced by asymmetric charge distribution can lower dipole-dipole repulsion between the adjacent polarized  $\text{CO}^*$  intermediates, in which C atoms with positive charges will naturally repel one another. Hence, it boosts the C–C coupling.  $d_1$  is shorter than  $d$ . b Over a non-charge-ordered catalyst, repulsion hinders the C–C coupling.  $d_2$  is longer than  $d$ . Label: yellow ball: active sites; different colored rings outside the yellow ball represent different valence states of the same metal site; red ball: oxygen atom; grey ball: carbon atom; dotted circle: charge density; radius represents the corresponding value;  $d$ : the distance between two active sites;  $d_1$ : the distance between C atom adsorbed on charge-ordered dual sites;  $d_2$ : the distance between C atom adsorbed on non-charge-ordered dual sites.

argon atmosphere using Schlenk line. The solution was heated to 45 °C and kept for 1 hour under strong magnetic stirring. BHT (0.25 mM) was added to the solution. The mixture gradually became a dark blue suspension. After being stirred at 45 °C for 48 hours in an oil bath, the solid products were collected by filtration and washed with dimethylformamide, acetonitrile, and methanol in sequence. This product was dried under 40 °C with a dynamic vacuum for 24 h. Cu4BHT was obtained as a dark blue powder (110 mg, Yield 84.8%).

## 2.2. Material characterization

X-ray diffraction measurements were performed on a Rigaku Smart Lab powder X-ray diffractometer (XRD) operated at 9 kW with Cu  $K\alpha$  radiation ( $\lambda = 1.5418 \text{ \AA}$ ). The in-situ XRD has been conducted with a homemade device on the same diffractometer [31]. We performed scanning transmission electron microscopy (STEM) imaging and energy-dispersive X-ray spectroscopy (EDS) analysis on an FEI Titan Themis apparatus with an X-FEG electron gun and a DCOR aberration corrector operating at 300 kV. TEM images were obtained on a Cryogenic-TEM under a liquid-nitrogen temperature (77 K) environment. The X-ray photoelectron spectroscopy (XPS) was operated on the PHI 5000 Versaprobe III system. X-ray absorption spectra (XAS) on the Cu K edge were obtained at 7D XAFS beamline with ionized chamber detectors of the Pohang Accelerator Laboratory (PAL), using a Si (111) double crystal monochromator. Analyses of the XANES and EXAFS were performed using Athena software [32]. In-situ attenuated total reflection ATR-FTIR spectra were carried out using a Bruker Vertex 80 infrared spectrometer provided with a liquid nitrogen-cooled RT-DLaTGS detector and a homemade spectro-electrochemical cell [33]. To prepare the bulk compounds after electrolysis for TEM, the fresh electrode for the electrocatalyst was prepared without adding a binder to eliminate ambiguous interference. After 1 h electrolysis, the catalyst and gas diffusion layer (GDL) were quickly transported into an argon-filled glove box to get rid of oxygen. The sample was then slightly scraped off, dispersed in ethanol, and dropped onto a Quantifoil carbon TEM grid. For the rest of the HRTEM and EDS measurements, we prepared samples on a lacey carbon TEM grid.

## 2.3. COR experiments

### 2.3.1. Working electrode preparation

A homogeneous catalyst ink was first prepared by blending 6 mg of catalyst in 1 mL of ethanol and 50  $\mu\text{L}$  of Nafion solution (5% in ethanol), and followed by ultrasonication for 0.5 h. Then, the ink was sprayed onto a GDL (2 cm  $\times$  3 cm) electrode (Sigracet 29 BC, Fuel Cell Store). The amount of loaded catalysts is set to be 1 mg  $\text{cm}^{-2}$ .

### 2.3.2. Flow cell CO electrolysis

Electrochemical CO reduction reaction was evaluated in 1.0 M KOH solution in a microfluidic flow cell electrolyzer. The dimensions of the flow chamber was 2 cm  $\times$  0.5 cm  $\times$  0.15 cm. The flow rate of the supplied  $\text{CO}_2$  was 20 sccm (standard cubic centimeter per minute), which was controlled by a mass flow controller (ALICAT). The flow rate of the electrolyte was controlled at 5  $\text{mL min}^{-1}$  via a peristaltic pump. The anode and cathode chambers were separated by an anion exchange membrane (FAA-3, Fumatech). An  $\text{IrO}_2$ -coated titanium plate served as the counter electrode in the anode chamber. All the potentials were recorded against a leak-free Ag/AgCl reference electrode and converted to the reversible hydrogen electrode (RHE) reference scale using  $E$  (vs. RHE) =  $E$  (vs. Ag/AgCl) + 0.197 V + 0.0591  $\times$  pH without iR compensation. The chronopotentiometry measurements were conducted at different potentials with a potentiostat (CHENHUA, CHI760E). The linear sweep voltammetry (LSV) was collected at a scan rate of 20 mV  $\text{s}^{-1}$ . The electrolysis products at each potential were quantified over 1000 s and repeated at least three times. The gaseous products were quantified by online multiple gas chromatography (Fuli GC9790P)

equipped with 5 Å molecular sieve, Hayesep A, and Porapak N columns.  $\text{H}_2$  was quantitatively analyzed by a thermal conductivity detector. A flame ionization detector was used to quantify methane and ethylene. The integral peak area of the reduced product was used to calculate the concentration of gaseous products. The Faraday efficiency (FE) of gas-phase products was calculated by the following equation:

$$\text{FE}(\%) = \frac{\left( \frac{\nu}{60 \text{ s/min}} \right) \times \left( \frac{y}{24000 \text{ cm}^3/\text{mol}} \right) \times N \times F}{j} \times 100\%$$

Where  $\nu$  is the CO gas flow rate (sccm),  $y$  is the measured concentration of product detected by GC,  $N$  is the number of transfer electrons for producing a molecule of CO or  $\text{H}_2$ ,  $F$  is the Faraday constant (96,485 C mol $^{-1}$ ),  $j$  is the recorded current (A). The FE (%) for the gas-phase products reported were the average values of three tests during single electrolysis.

liquid products were detected using  $^1\text{H}$  NMR spectroscopy (Bruker AVII 400 MHz): 0.4 mL of the electrolyte was mixed with 50  $\mu\text{L}$  80 ppm of dimethyl sulfoxide (internal standard) and 50  $\mu\text{L}$  of deuterated water. The FE of liquid-phase products was calculated as follows:

$$\text{FE} = \frac{nf}{Q}$$

Where  $n$  is the mole amount of the liquid product,  $F$  is the Faraday constant (96485 C mol $^{-1}$ ),  $Q$  is the total electric charge passed through the electrode.

## 2.4. Density functional theory calculations

Considering the XRD analysis, (111) plane for Cu4BHT and (001) plane for Cu3BHT were found to be pre-orientation that might be easily exposed to the outer surface. Thus, these two surfaces were considered in the DFT calculation. Spin-polarized density functional theory (DFT) calculations were carried out using the Cambridge Serial Total Energy Package (CASTEP) code [34]. The electron exchange-correlation potential was performed using Perdew-Burke-Ernzerhof (PBE) functional of generalized gradient approximation (GGA) [35]. Meanwhiles, the ultrasoft pseudopotentials were employed. The kinetic energy cutoff was set to 500 eV for the plane-wave basis set. Brillouin zone integration was sampled with  $4 \times 4 \times 4$ ,  $4 \times 4 \times 3$  and  $3 \times 3 \times 1$  Monkhorst Pack mesh  $k$ -point for bulk Cu3BHT, Cu4BHT and their surface models, respectively. For Cu3BHT and Cu4BHT surface models, a vacuum region of 15  $\text{\AA}$  along with the  $z$ -axis was used to prevent interactions between adjacent layers. Tkatchenko-Scheffler (TS) scheme was used to describe the van der Waals (vdW) interactions [35]. To evaluate the C–C coupling on Cu4BHT surface for  $\text{C}_2$  production, synchronous transit methods with completed linear synchronous transit (LST) and quadratic synchronous transit (QST) were utilized [36]. The outer valence electron arrangement of each element was  $1s^1$  for H,  $2s^22p^2$  for C,  $2s^22p^4$  for O,  $3s^23p^4$  for S and  $3d^{10}4s^1$  for Cu respectively. The convergence tolerances were set to be  $1 \times 10^{-5}$  eV per atom for energy,  $1 \times 10^{-3}$   $\text{\AA}$  for maximum displacement, and 0.03 eV  $\text{\AA}^{-1}$  for maximum force. All of the structures were fully optimized and relaxed to the ground state. The adsorption energy ( $E_{ads}$ ) of PDS on the NCP surface was calculated as follow:

$$E_{ads} = E_{Surf+PDS} - E_{Surf} - E_{PDS}$$

The change in Gibbs free energy ( $\Delta G$ ) for each of the CORR steps was evaluated reference to the computational hydrogen electrode (CHE) model in literature [37,38]. The Gibbs free energy was defined as:

$$\Delta G = \Delta E_{DFT} + \Delta E_{ZPE} - T\Delta S$$

Where  $\Delta E_{DFT}$  is the electronic energy difference directly obtained from DFT calculation,  $\Delta E_{ZPE}$  and  $T\Delta S$  are the zero-point energy correction and entropy change at 298.15 K, respectively. In addition, since the PBE function can not describe this molecule accurately,  $-0.41$  eV correction was applied to the electronic energy of CO [38,39].

### 3. Results and discussion

#### 3.1. Catalyst synthesis and structural characterization

The charge-ordered Cu4BHT was synthesized via a one-pot hydrothermal process by engaging benzenehexathiol (BHT) with tetrakis (acetonitrile)copper(I) tetrafluoroborate ( $[\text{Cu}(\text{CH}_3\text{CN})_4]\text{BF}_4$ ) and Copper(II) acetate monohydrate( $\text{Cu}(\text{CH}_3\text{COO})_2 \cdot \text{H}_2\text{O}$ ), according to the documented procedure [30]. Powder X-ray diffraction (XRD) patterns corroborate the high purity of the as-synthesized Cu4BHT material (Fig. 2a), crystallizing in the space group of  $P\bar{1}$  (CCDC No.2015799) [30]. The high-resolution transmission electron microscopy (HRTEM) image in Fig. 2b shows a lattice spacing of 0.350 nm, ascribed to the crystallographic (111) lattice plane of Cu4BHT. The energy dispersive X-ray spectroscopy (EDS) mapping confirms the even distribution of Cu and S within the crystal (Fig. S1). Copper K-edge Fourier-transformed extended X-ray absorption fine structure (FT-EXAFS) spectroscopy was used to evaluate the first coordination sphere around copper atoms (Fig. 2c). Cu4BHT exhibits only one prominent peak at 2.17 Å (phase correction is implemented), which can be assigned to Cu-S backscattering. FT-EXAFS result indicates the Cu atom is coordinated with S atoms, which is consistent with the crystal structure analysis result (Fig. S5b). Moreover, compared with the wavelet transform (WT) plot of Cu foil, no intensity maximum is detected near 7.5 Å<sup>-1</sup> (corresponding to the Cu-Cu path), providing evidence for the atomic dispersion of Cu atoms (Fig. S6). High-resolution XPS spectra and valence bond sum (BVS) calculation were employed to elucidate the chemical state of the Cu atom. As shown in Fig. 2d-bottom, in addition to peaks ascribed to  $\text{Cu}^{2+}$ , which locate at 954.6 and 934.5 eV, peaks corresponding to  $\text{Cu}^+$

appear at 952.4 and 932.7 eV in the Cu 2p XPS spectrum with a  $\text{Cu}^+/\text{Cu}^{2+}$  ratio of  $\sim 1$  [20]. Furthermore, X-ray absorption near-edge structure (XANES) spectra (Fig. 2e and Fig. S7) of Cu4BHT reveal that the position of 1s-4p transition peak for Cu4BHT (8978.91 eV) is located between CuS (8979.83 eV) and Cu<sub>2</sub>O (8977.78 eV). The results demonstrate that two aliovalent Cu atoms are presented in Cu4BHT frameworks. One Cu atom, denoted as Cu<sub>A</sub>, is located in a square planar coordinational configuration; the other one, denoted as Cu<sub>B</sub>, is coordinated with three sulfur atoms to form a planar trigonal geometry (Fig. S5b). According to BVS calculation [40], Cu<sub>A</sub> and Cu<sub>B</sub> are in the valence state of 2.17+ and 1.08+, respectively, implying that the charge-ordered Cu<sup>+</sup>/Cu<sup>2+</sup> dual-site pair is involved within the framework. Mulliken charge analysis based on density functional theory (DFT) in Fig. 2f shows that the Cu<sub>B</sub> site in the Cu4BHT structure possesses a lower charge density of 0.34 relative to the Cu<sub>A</sub> sites (0.42–0.43), which verifies the asymmetric charge distribution feature on charge-ordered copper dual-site pair [41].

For comparison, Cu-based non-charge-ordered MOF, Cu3BHT, has also been synthesized with Cu<sup>2+</sup> precursor [29]. The as-synthesized material was carefully characterized, as shown in Fig. S2–S4. The structural building units in Cu3BHT are partially similar to those in Cu4BHT, apart from all the Cu atoms with the chemical state of 2+ (Fig. 2c–e, Fig. S5 and S7). The Mulliken analysis in Fig. 2f further reveals the feature of symmetric charge distribution character in non-charge-ordered Cu3BHT.

#### 3.2. COR performance in alkaline electrolyte

The unique electronic structure of the periodic arrangement of Cu<sup>+</sup>/

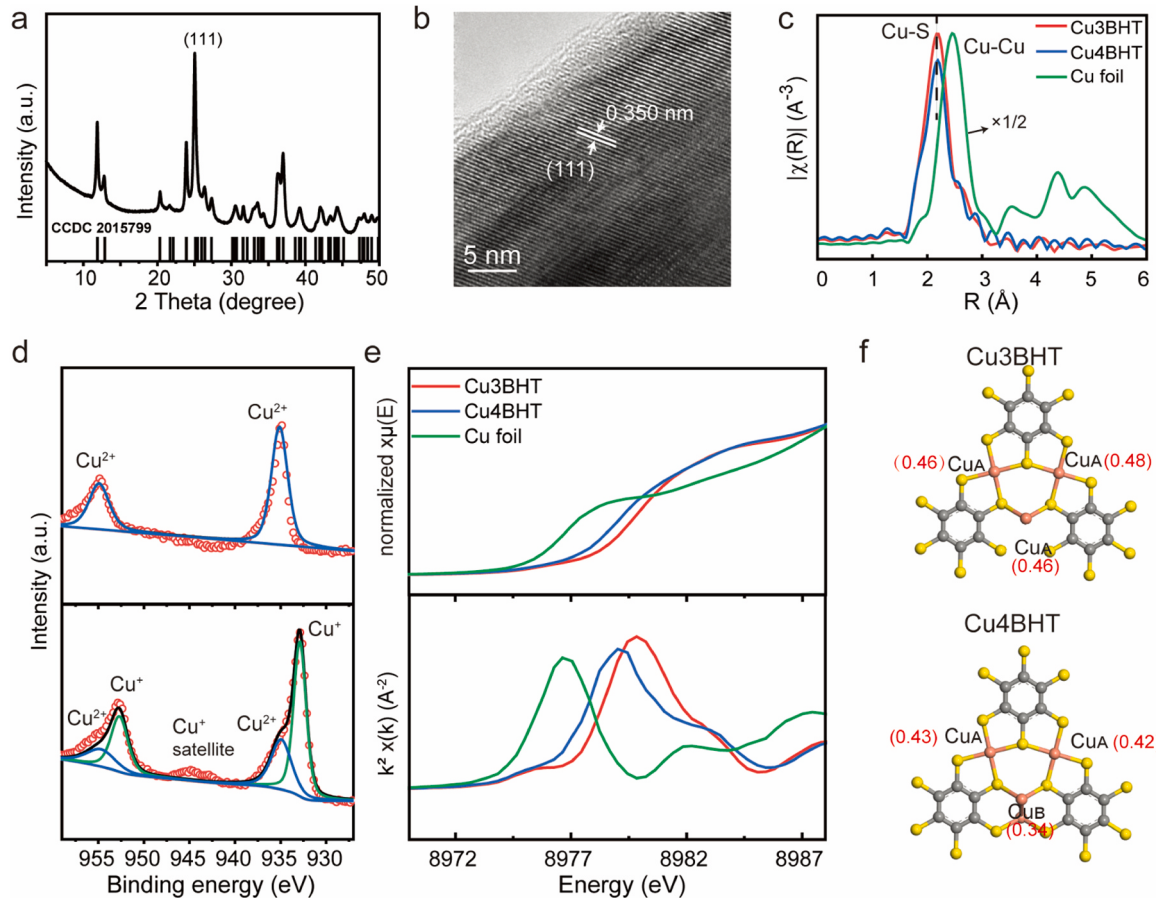


**Fig. 2.** Structure characterization. **a** XRD of as-synthesized Cu4BHT. **b** HRTEM image of Cu4BHT. **c** Normalized Fourier transformed magnitudes of K-edge EXAFS signals of as-synthesized Cu4BHT, Cu3BHT, and Cu foil. **d** XPS spectra of Cu 2p of Cu4BHT (bottom) and Cu3BHT (top). **e** Cu K-edge XANES spectra (top) and their first derivative curves (bottom) of Cu4BHT, Cu3BHT and Cu foil. **f** Mulliken population of Cu4BHT (bottom), and Cu3BHT (top).

$\text{Cu}^{2+}$  atoms pair provides excellent feasibility to enhance CO adsorption affinity and boost C–C coupling [25]. Accordingly, it is promising to employ Cu4BHT for CO electroreduction reaction. The COR measurements were evaluated in a microfluidic flow cell reactor with 1.0 M KOH aqueous solution electrolyte. The recorded potentials were converted to the reversible hydrogen electrode unless otherwise specified. From the linear sweep voltammetry (LSV) curves (Fig. 3a), Cu4BHT renders a much higher current density at the applied potential range of  $-0.7 \text{ V} \sim -1.2 \text{ V}$  under CO feeding, compared with non-charge-ordered Cu3BHT (Fig. S8a). Moreover, a prominent current density enhancement was identified in CO-purged over Ar-fed LSV for the Cu4BHT electrode, suggesting a potential favorable COR response of Cu4BHT. Fig. 3b and Fig. S8b show faradaic efficiencies (FE) of COR product distributions as a function of the applied potentials for Cu4BHT and Cu3BHT, respectively. Over Cu4BHT, besides  $\text{CH}_4$ , the  $\text{C}_2$  products of ethylene, acetate and ethanol were also obviously detected (Fig. 3b and Fig. S9). At the applied potential of  $-0.7 \text{ V}$ , acetate was produced preferentially than others among the  $\text{C}_2$  products, and a markedly high acetate FE of 50.3% was achieved accompanied by an ultrahigh liquid product purity of 95.6%. Such excellent acetate FE is among the top of selectivity from CO to acetate (Fig. 3c, d and Table S1). The acetate selectivity was still maintained  $>40\%$  at  $-0.8 \text{ V}$ ; after this threshold, the corresponding acetate production gradually declined, and the methane increased (Fig. 3b). In stark contrast, for Cu3BHT, due to the single Cu site tending to bind with only one CO molecule and hinder C–C coupling [42],  $\text{CH}_4$  is the dominant carbon product. Under this circumstance, an optimal FE

of 15.6% was achieved at the applied potential of  $-0.8 \text{ V}$ . As the potential shifted negatively, the  $\text{CH}_4$  selectivity gradually decreased; instead, the byproducts of  $\text{H}_2$  overwhelmed (Fig. S8b and S10). Further comparing the FE of total carbon products clearly shows a much higher carbon product contribution on Cu4BHT than that of Cu3BHT, indicating that Cu4BHT with charge-ordered  $\text{Cu}^+/\text{Cu}^{2+}$  sites pair effectively promotes carbon products generation and  $\text{C}_2$  product selectivity [26, 27].

The stability of the catalyst was further scrutinized by extensive in-situ and ex-situ characterizations. Cu4BHT was proved to be stable in 1.0 M KOH electrolyte, which showed good stability over 10 h electrolysis under high current intensity mode (Fig. S11a and b). In-situ XRD experiment under a CO atmosphere at  $-1.0 \text{ V}$  showed that no new diffraction peaks referring to copper clusters or other copper oxides were observed (Fig. S11c). To gain a deeper insight into the possible subatomic structure changes during the CORR, HRTEM image was taken from a cryogenic transmission electron microscope (Cryo-TEM), which shows Cu4BHT catalyst remains same morphology and lattice fringe after CORR (Fig. S11d-f and S12). No Cu-based clusters were observed, which indicates the CO reduction active sites are Cu atoms within Cu4BHT instead of a decomposed and reconstructed copper cluster. Quasi-situ  $\text{Cu} 2p$  XPS spectrum of Cu4BHT after 10 h electrolysis shows that a peak is located between the peak of  $\text{Cu}^{2+}$  and  $\text{Cu}^+$  (Fig. S11g), distinguished from the fresh Cu4BHT. As it is well known, CO molecule is easily adsorbed on Cu site. Thus, after 10 h electrolysis, there were abundant CO absorbed on the Cu4BHT surface via chemisorption, which

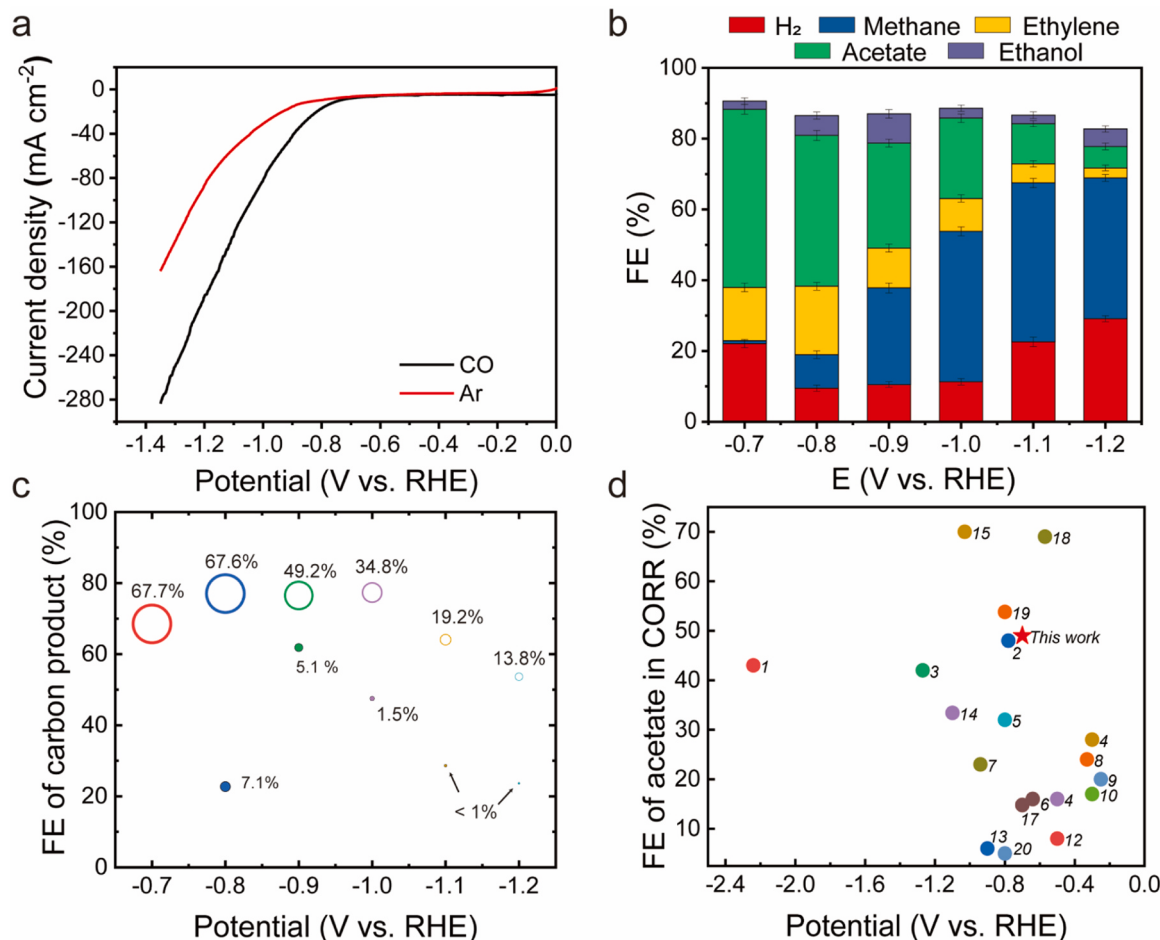


**Fig. 3.** Catalytic performance of CO reduction reaction (CORR). **a** LSV curves of Cu4BHT under argon or CO gas feeding. **b** FE towards  $\text{H}_2$  and CO reduction products on Cu4BHT. **c** FE of total carbon products at different applied potentials over Cu4BHT (hollow circles) and Cu3BHT (filled circles). The diameter of the circle indicates the percentage references for the FE of total  $\text{C}_2$  products. **d** FE of acetate production in CORR compared to the literature work. Numbers refer to previously reported catalysts summarized in Table S1.

modified the charge density distribution of these sites, as the electrons transferred from Cu site to CO. Accordingly, the XPS peak of Cu site shifted. The electrons transfer process and charge density rearrangement of  $\text{Cu}_B^+/\text{Cu}_A^{2+}$  dual sites were elucidated by DFT calculation and discussed below. However, S 2p XPS spectra show no changes in binding energy, further indicating a stable copper coordination structure (Fig. S13). Taken together, the as-prepared Cu4BHT is stable enough under sustained catalytic turnover.

### 3.3. Structural insights of CO to $\text{C}_2$ catalytic activity

To explore the potential reaction pathways on these catalysts for CO reduction. The reaction dynamics of CO electroreduction to  $\text{C}_2$  products on Cu4BHT were tracked via in-situ ATR-FTIR measurements (Fig. 4a and b). No apparent CO adsorption band is located at the spectral region of 1750–2000  $\text{cm}^{-1}$ , but two CO adsorption peaks at 2170 and 2115  $\text{cm}^{-1}$  are observed, verifying the linear adsorbed CO configuration (Fig. 4a) [43,44]. The two linear adsorbed CO on the Cu4BHT surface suggest two types of CO adsorption sites, which is robust evidence to illustrate the charge-ordered Cu site pair ( $\text{Cu}_B^+/\text{Cu}_A^{2+}$ ) in the Cu4BHT structure [43–45]. As comparison, over non-charge-ordered Cu3BHT, only one linear CO adsorption peak is observed (Fig. S14). In addition, the FTIR spectra of Cu3BHT show a relatively weaker CO adsorption than Cu4BHT, taking O–H stretching vibration band at  $\sim 3298 \text{ cm}^{-1}$  and bending vibration adsorption peak at 1622  $\text{cm}^{-1}$  as references [46, 47].

The bands at 1464 and 1323  $\text{cm}^{-1}$  are associated with the  $\text{OCCO}^*$  group, a typical CO\* coupling product [48,49]. Additionally, the C–OH stretching band at 1184  $\text{cm}^{-1}$  and the C=O stretching band at 1691  $\text{cm}^{-1}$  indicate the presence of key intermediates  $^*\text{COCOH}$  towards  $\text{C}_2$  products [48,50]. The most prominent band at 1527  $\text{cm}^{-1}$  that is slightly weakened when the potential increase could be attributed to O–C=O, indicative of a good agreement with COR performance of yielding  $\text{CH}_3\text{COOH}$  (Fig. 4b) [48]. The weaker band at 1065  $\text{cm}^{-1}$  can be ascribed to the H–C=O nonplanar vibration of the  $^*\text{CHO}$ , which is the key intermediate for ethanol production [50]. In addition, the intermediate ( $\text{CH}_3\text{O}^*$  peak at 1120  $\text{cm}^{-1}$ ) towards  $\text{CH}_4$  formation was also

observed on Cu4BHT surface with increasing the applied potential [50]. According to the in-situ FTIR spectra results, it deduces that adsorbed  $^*\text{CO}$  on Cu4BHT converts to  $\text{OCCO}^*$  intermediate and then generates key intermediate  $^*\text{COCOH}$  that participates in  $\text{C}_2$  products formation (acetic acid, ethanol, ethylene) under electric force (Fig. 4c).

To uncover the intrinsic mechanism for outstanding COR performance and  $\text{C}_2$  selectivity over the charge-ordered  $\text{Cu}^+/\text{Cu}^{2+}$  sites pair, DFT calculations were performed. The CO adsorption behavior was first evaluated. We chose Cu4BHT (111) and Cu3BHT (001) as the catalyst active surface based on the results of XRD strongest diffraction and surface energy optimization. DFT calculation shows that the CO adsorption energy on Cu4BHT (111) surface is much more negative compared with that on Cu3BHT (001) (Table S2), indicating an easier CO adsorption on charge-ordered Cu site in Cu4BHT (111) surface. This observation is consistent with the result of in-situ IR spectra observation. Significantly, the charge density on charge-ordered Cu sites ( $\text{Cu}_B^+/\text{Cu}_A^{2+}$ ) is rearranged with equal distribution feature after CO adduct (Fig. S15), indicating that the charge-ordered Cu pair induced electronic field is conducive to the CO adsorption. The charge density of  $\text{Cu}_B^+$  increased markedly from 0.34 to 0.42, while  $\text{Cu}_A^{2+}$  remained unchanged. This feature of even charge density distribution is in accord with characteristic of Cu 2p XPS spectrum of used Cu4BHT (Fig. S11g), in which  $\text{Cu}_B$  and  $\text{Cu}_A$  show an identical peak locating between the peaks of  $\text{Cu}^+$  and  $\text{Cu}^{2+}$ . After adsorption, the electron on Cu atoms could be transferred to the adsorbed CO, weakening the C–O bond, and facilitating the catalysis process (Fig. S16). In reverse, weaker binding implies rapid desorption of  $^*\text{CO}$  on the Cu3BHT surface, leaving little opportunity for further reduction reaction [51].

The CO bonding nature on different Cu sites of Cu4BHT and Cu3BHT was further studied by the electron localization function (ELF) and crystal orbital Hamilton population (COHP). On the Cu4BHT (111) surface, ELF diagram shows a clear electron localization feature between Cu atom and C atom after CO adsorption (Fig. 5a). While on Cu3BHT (001) surface, ELF diagram shows that most electron density of CO molecules is localized on carbon atoms, indicating the unlike activation of CO molecules (Fig. S17). In addition, the COHP further verifies the anti-bond orbital filling of C–O\* on Cu4BHT is significantly higher than

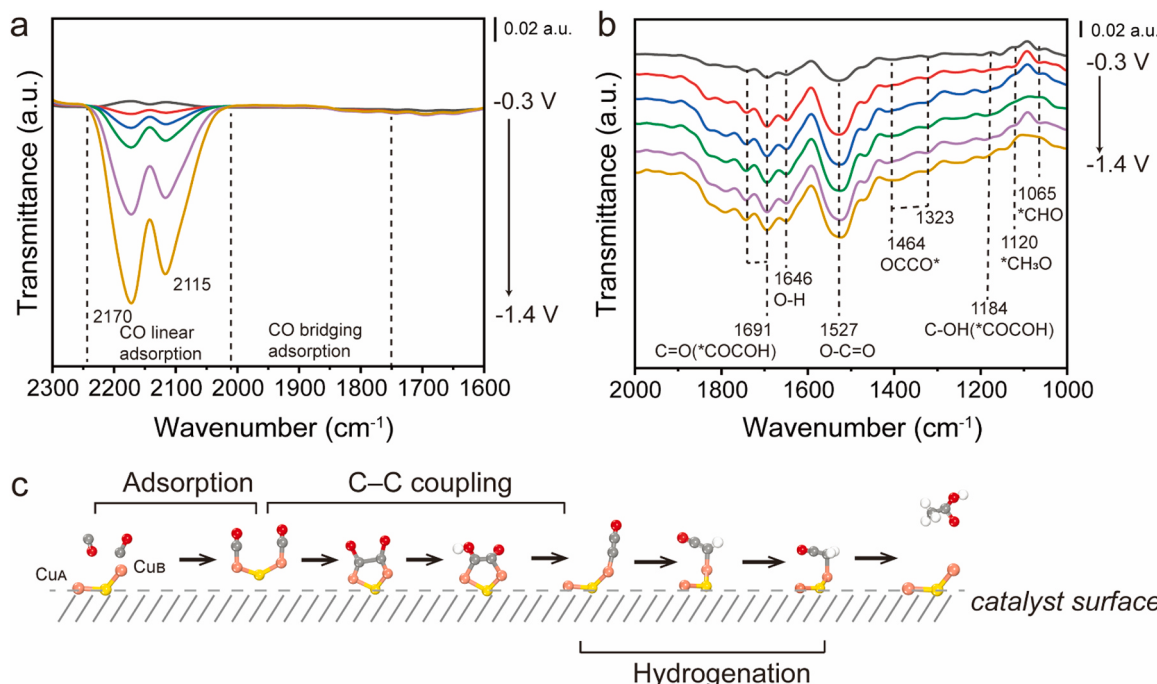
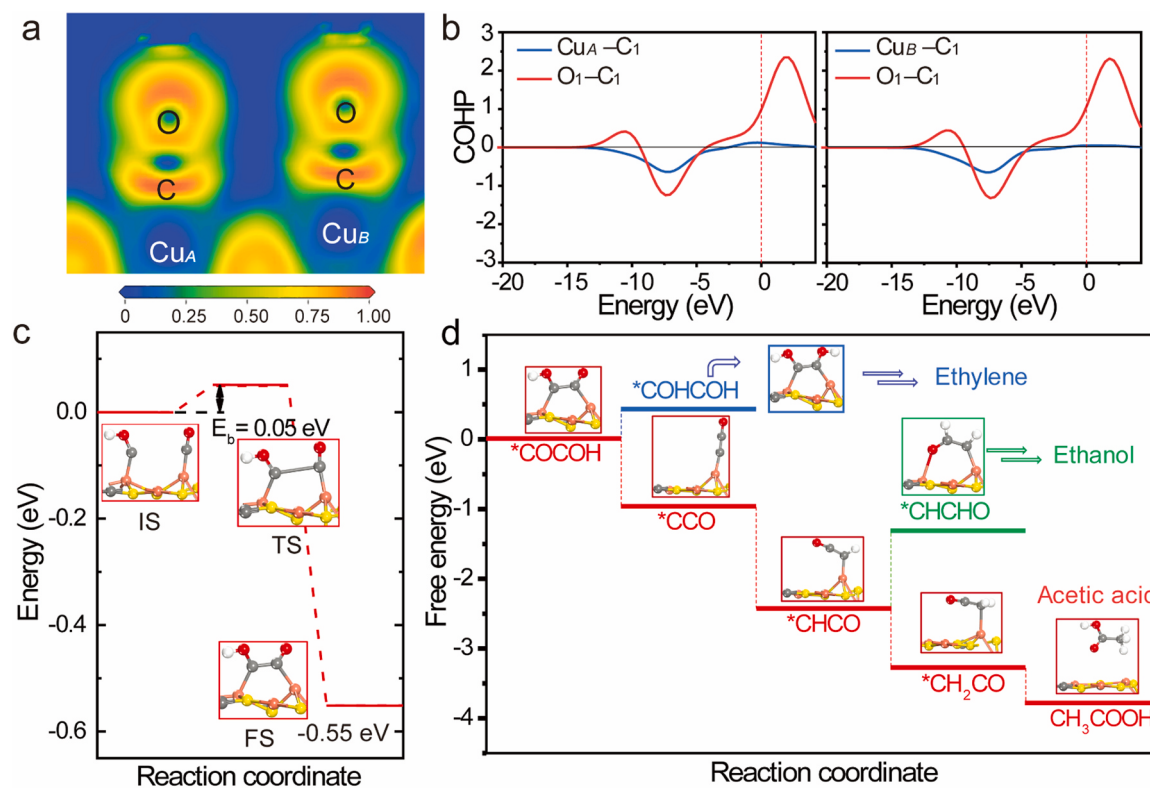


Fig. 4. Reaction dynamics of CORR. a, b In-situ ATR-IR spectra of Cu4BHT during the electrochemical CORR. c Schematic diagram of CO reduction to acetate on Cu4BHT.



**Fig. 5.** Structural insights of CO to C<sub>2</sub> catalytic activity. **a** Electron localization function (ELF) plots of two CO molecules adsorbed on adjacent Cu<sub>A</sub> atom and Cu<sub>B</sub> atom on Cu4BHT. **b** Crystal orbital Hamilton population (COHP) in CO adsorbed models of Cu4BHT. **c** Calculated energy diagram for C—C coupling process on Cu4BHT. **d** Gibbs free energy calculations towards the reaction pathways. The blue, green, and red lines show the reaction pathways of CORR to ethylene, ethanol, and acetic acid, respectively.

Cu3BHT, indicating the successful C=O bond activation on Cu4BHT surface (Fig. 5b and Fig. S18) [52].

To study the C—C coupling mechanisms, we chose \*COCOH as the key intermediate based on our in-situ IR result and literature reports [53–56]. Kinetic barriers of reaction intermediates suggest that \*CO dimerization is kinetically favorable on Cu4BHT (111) surface (Fig. 5c). To reveal the relationship between the charge-ordered Cu<sub>B</sub><sup>+</sup>/Cu<sub>A</sub><sup>2+</sup> dual sites and COR selectivity on acetate production on Cu4BHT, Gibbs free energy calculations were implemented, and the result is shown in Fig. 5d. \*COHCOH and \*CCO are two predominant intermediates derived from \*COCOH. When the proton-coupled electron transfer (PCET) process occurs on \*COCOH, intermediate \*COHCOH forms, and results in the formation of C<sub>2</sub>H<sub>4</sub> as the final product with a slightly increased free energy barrier of 0.44 eV. When C—OH bond is dissociated from \*COCOH instead of the PCET process, another type of intermediate \*CCO could be formed, with a decreased free energy of −0.96 eV. Obviously, the dissociation of C—OH bond from \*COCOH intermediate is favorable on the Cu4BHT surface compared with the PCET process, leading to the trace production of C<sub>2</sub>H<sub>4</sub>, which is consistent with our experimental results (5% C<sub>2</sub>H<sub>4</sub> yield in overall C<sub>2</sub> production at low potential).

The formation of \*CHCHO versus \*CH<sub>2</sub>CO from \*CHCO is the key branching point in determining the selectivity towards ethanol versus acetic acid. The hydrogenation process on the terminal C site in \*CHCHO could result in ethanol formation, increasing free energy ( $\Delta G = 1.12$  eV). In reverse, the hydrogenation process that occurs at the bridge C site in \*CHCO is an energy decrease process ( $\Delta G = -1.35$  eV), forming the critical intermediate ketene (\*CH<sub>2</sub>CO) for acetic acid generation (Fig. 5d). The Cu<sub>B</sub> atom site in Cu4BHT with higher electron-donating ability promotes hydrogenation on bridge carbon in the \*CHCO intermediate, which induces the product selectivity towards acetic acid (Fig. 5d and Fig. S19). Theoretical modeling results indicate

the charge-ordered Cu dual-site pair presents outstanding selectivity of acetic acid generation over ethanol, matching well with the COR experimental result.

Based on above experimental and theoretical results, we propose the charge-ordering Cu dual-site play multi-role on contributing the high acetate production selectivity: (1) On the CO adsorption step, a combination of Cu<sup>2+</sup>—Cu<sup>+</sup> dual site shows better CO binding behavior, the Cu<sup>2+</sup> active site deviate from its original square planar panel, and the Cu<sup>+</sup> active site present better charge transfer ability from Cu to CO; (2) at C—C coupling step, the electrostatic interaction induced by asymmetric charge distribution lower the dipole-dipole repulsion, manifesting as the off-plane behavior from Cu<sup>2+</sup> site. This shortens the distance between two adsorbed CO, facilitating the C—C coupling step; (3) the theoretical study shows, on the C<sub>2</sub> products pathway, when this off-planed Cu<sup>2+</sup> site delivered CO to Cu<sup>+</sup>—CO intermediate, Cu<sup>2+</sup> trend to recover to its square planar geometry. This charge ordering dual site inhibit the formation of Cu—O bond as well as the generation of the key intermediate \*CHCHO, thereafter undermine the FE of ethanol, resulting a high selectivity to acetate.

#### 4. Conclusions

In summary, to accelerate the critical C—C coupling step during CO<sub>2</sub>/CO electroreduction to C<sub>2</sub> products, we propose and validate that the charge-ordered site pair is conducive to facilitating the C<sub>2</sub> products formation. As a proof of concept, Cu-based MOF Cu4BHT with long-range charge-ordered Cu<sup>+</sup>/Cu<sup>2+</sup> site pair has been successfully constructed and employed for the catalytic reaction, which fosters a preferential electroreduction of CO to C<sub>2</sub> products. A superior acetate selectivity of 50.3% (liquid products selectivity up to 95%) is delivered by Cu4BHT at −0.7 V versus RHE. Moreover, under −0.8 V versus RHE, the Cu4BHT exhibits tenfold enhancement of C<sub>2</sub> product formation than

that of Cu3BHT with non-charge-ordered single Cu sites. Detailed theoretical investigations combining in-situ ATR-FTIR analysis suggest a favorable CO adsorption on the charge-ordered  $\text{Cu}^+/\text{Cu}^{2+}$  sites owing to electrostatic interaction induced by asymmetric charge distribution. On the charge-ordered  $\text{Cu}^+/\text{Cu}^{2+}$  sites, charge rearrangement occurs after CO adsorption, which lowers the C-C coupling energy barriers for  $\text{C}_2$  product formation. Indeed, some localized and short-range charge-ordered site pairs also exist in the reported works with relatively high  $\text{C}_2$  products selectivity, like  $\text{Cu}^0/\text{Cu}^+$  site pairs on the  $\text{Cu}/\text{Cu}_2\text{O}$  interface and dopant-induced  $\text{Cu}^0/\text{Cu}^{\delta+}$  site pairs, but they are not noticed [5,15, 57,58]. It suggests that charge-ordering might be a universal strategy for electronic structure regulation and can be extended to designing other catalysts with outstanding activity and selectivity towards long-chain carbon fuel production. This work not only reports a new electrocatalyst with excellent selectivity for acetate production, but also provides a novel insight for rational design electrocatalysts from electron density engineering of local catalytic active sites.

#### CRediT authorship contribution statement

**Wei Xu:** Investigation. **Lele Duan:** Writing – review & editing, Supervision. **Hong Chen:** Writing – review & editing, Supervision, Funding acquisition, Conceptualization. **Siyuan Luo:** Writing – original draft, Investigation, Funding acquisition. **Haiyuan Zou:** Investigation. **Renji Zheng:** Investigation. **Shimao Deng:** Writing – review & editing. **Xuezhen Feng:** Investigation. **Wenfei Wei:** Investigation. **Ranhai Wang:** Investigation. **Ze Li:** Investigation.

#### Declaration of Competing Interest

The authors declare that they have no known competing financial interests or personal relationships that could have appeared to influence the work reported in this paper.

#### Data Availability

Data will be made available on request.

#### Acknowledgements

This work was financially supported by the Shenzhen Science and Technology Innovation Committee (KCXST20221021111208018, H.C.), National Natural Science Foundation of China (No. 22006065, S.L.), Guangdong Basic and Applied Basic Research Foundation, China (No. 2019A1515111092, S.L.). We acknowledge the beamline scientist Sun Hee Choi at Pohang Accelerator Laboratory (PAL) helped with the XAS data acquirement. We also acknowledge the technical support from the SUSTech Core Research Facilities and Centre for Computational Science and Engineering at Southern University of Science and Technology.

#### Appendix A. Supporting information

Supplementary data associated with this article can be found in the online version at [doi:10.1016/j.apcatb.2024.123887](https://doi.org/10.1016/j.apcatb.2024.123887).

#### References

- [1] L. Fan, C. Xia, F. Yang, J. Wang, H. Wang, Y. Lu, Strategies in catalysts and electrolyzer design for electrochemical  $\text{CO}_2$  reduction toward  $\text{C}_{2+}$  products, *Sci. Adv.* 6 (2020) 1–18, <https://doi.org/10.1126/sciadv.ayy3111>.
- [2] M. Jouny, W. Luc, F. Jiao, High-rate electroreduction of carbon monoxide to multi-carbon products, *Nat. Catal.* 1 (2018) 748–755, <https://doi.org/10.1038/s41929-018-0133-2>.
- [3] S. Nitopi, E. Bertheussen, S.B. Scott, X. Liu, A.K. Engstfeld, S. Horch, B. Seger, I.E. L. Stephens, K. Chan, C. Hahn, J.K. Nørskov, T.F. Jaramillo, I. Chorkendorff, Progress and Perspectives of electrochemical  $\text{CO}_2$  reduction on copper in aqueous electrolyte, *Chem. Rev.* 119 (2019) 7610–7672, <https://doi.org/10.1021/acs.chemrev.8b00705>.
- [4] W. Ye, X. Guo, T. Ma, A review on electrochemical synthesized copper-based catalysts for electrochemical reduction of  $\text{CO}_2$  to  $\text{C}_{2+}$  products, *Chem. Eng. J.* 414 (2021) 128825, <https://doi.org/10.1016/j.cej.2021.128825>.
- [5] W. Liu, P. Zhai, A. Li, B. Wei, K. Si, Y. Wei, X. Wang, G. Zhu, Q. Chen, X. Gu, R. Zhang, W. Zhou, Y. Gong, Electrochemical  $\text{CO}_2$  reduction to ethylene by ultrathin  $\text{CuO}$  nanoplate arrays, *Nat. Commun.* 13 (2022) 1–12, <https://doi.org/10.1038/s41467-022-29428-9>.
- [6] D. Raciti, C. Wang, Recent advances in  $\text{CO}_2$  reduction electrocatalysis on copper, *ACS Energy Lett.* 3 (2018) 1545–1556, <https://doi.org/10.1021/acsenergylett.8b00553>.
- [7] P.P. Yang, X.L. Zhang, F.Y. Gao, Y.R. Zheng, Z.Z. Niu, X. Yu, R. Liu, Z.Z. Wu, S. Qin, L.P. Chi, Y. Duan, T. Ma, X.S. Zheng, J.F. Zhu, H.J. Wang, M.R. Gao, S.H. Yu, Protecting copper oxidation state via intermediate confinement for selective  $\text{CO}_2$  electroreduction to  $\text{C}_{2+}$  fuels, *J. Am. Chem. Soc.* 142 (2020) 6400–6408, <https://doi.org/10.1021/jacs.0c01699>.
- [8] P. De Luna, R. Quintero-Bermudez, C.T. Dinh, M.B. Ross, O.S. Bushuyev, P. Todorović, T. Regin, S.O. Kelley, P. Yang, E.H. Sargent, Catalyst redeposition controls morphology and oxidation state for selective carbon dioxide reduction, *Nat. Catal.* 1 (2018) 103–110, <https://doi.org/10.1038/s41929-017-0018-9>.
- [9] K.D. Yang, W.R. Ko, J.H. Lee, S.J. Kim, H. Lee, M.H. Lee, K.T. Nam, Morphology-directed selective production of ethylene or ethane from  $\text{CO}_2$  on a Cu mesopore electrode, *Angew. Chem.* 129 (2017) 814–818, <https://doi.org/10.1002/ange.201610432>.
- [10] R. Kas, K.K. Hummadi, R. Kortlever, P. De Wit, A. Milbrat, M.W.J. Luitjen-Olieman, N.E. Benes, M.T.M. Koper, G. Mul, Three-dimensional porous hollow fibre copper electrodes for efficient and high-rate electrochemical carbon dioxide reduction, *Nat. Commun.* 7 (2016), <https://doi.org/10.1038/ncomms10748>.
- [11] K. Wang, D. Liu, P. Deng, L. Liu, S. Lu, Z. Sun, Y. Ma, Y. Wang, M. Li, B.Y. Xia, C. Xiao, S. Ding, Band alignment in  $\text{Zn}_2\text{SnO}_4/\text{SnO}_2$  heterostructure enabling efficient  $\text{CO}_2$  electrochemical reduction, *Nano Energy* 64 (2019), <https://doi.org/10.1016/j.nanoen.2019.103954>.
- [12] P. Prabhu, V. Jose, J.M. Lee, Heterostructured catalysts for electrocatalytic and photocatalytic carbon dioxide reduction, *Adv. Funct. Mater.* 30 (2020) 1–32, <https://doi.org/10.1002/adfm.201910768>.
- [13] X. Feng, H. Zou, R. Zheng, W. Wei, R. Wang, W. Zou, G. Lim, J. Hong, L. Duan, H. Chen,  $\text{Bi}_2\text{O}_3/\text{BiO}_2$  nanoheterojunction for highly efficient electrocatalytic  $\text{CO}_2$  reduction to formate, *Nano Lett.* 22 (2022) 1656–1664, <https://doi.org/10.1021/acs.nanolett.1c04683>.
- [14] H. Lu, L. Li, Q. Wu, S. Mu, R. Zhao, X. Zheng, C. Long, Q. Li, H. Liu, C. Cui, Cu+-mediated CO coordination for promoting C-C coupling for  $\text{CO}_2$  and CO electroreduction, *ACS Appl. Mater. Interfaces* 15 (2023) 13228–13237, <https://doi.org/10.1021/acsami.3c01448>.
- [15] Y. Zhou, F. Che, M. Liu, C. Zou, Z. Liang, P. De Luna, H. Yuan, J. Li, Z. Wang, H. Xie, H. Li, P. Chen, E. Bladt, R. Quintero-Bermudez, T.K. Sham, S. Bals, J. Hofkens, D. Sinton, G. Chen, E.H. Sargent, Dopant-induced electron localization drives  $\text{CO}_2$  reduction to  $\text{C}_2$  hydrocarbons, *Nat. Chem.* 10 (2018) 974–980, <https://doi.org/10.1038/s41557-018-0092-x>.
- [16] Y. Jia, K. Jiang, H. Wang, X. Yao, The role of defect sites in nanomaterials for electrocatalytic energy conversion, *Chem* 5 (2019) 1371–1397, <https://doi.org/10.1016/j.chempr.2019.02.008>.
- [17] Q. Wang, Y. Lei, D. Wang, Y. Li, Defect engineering in earth-abundant electrocatalysts for  $\text{CO}_2$  and  $\text{N}_2$  reduction, *Energy Environ. Sci.* 12 (2019) 1730–1750, <https://doi.org/10.1039/c8ee03781g>.
- [18] A. Zhang, Y. Liang, H. Li, B. Zhang, Z. Liu, Q. Chang, H. Zhang, C.F. Zhu, Z. Geng, W. Zhu, J. Zeng, In-situ surface reconstruction of  $\text{mn}$  nanosheets for efficient  $\text{CO}_2$  electroreduction into formate, *Nano Lett.* 20 (2020) 8229–8235, <https://doi.org/10.1021/acs.nanolett.0c03345>.
- [19] W. Zhang, C. Huang, J. Zhu, Q. Zhou, R. Yu, Y. Wang, P. An, J. Zhang, M. Qiu, L. Zhou, L. Mai, Z. Yi, Y. Yu, Dynamic restructuring of coordinatively unsaturated copper paddle wheel clusters to boost electrochemical  $\text{CO}_2$  reduction to hydrocarbons, *Angew. Chem. - Int. Ed.* 61 (2022), <https://doi.org/10.1002/anie.20212116>.
- [20] Z.Q. Liang, T.T. Zhuang, A. Seifitakaldani, J. Li, C.W. Huang, C.S. Tan, Y. Li, P. De Luna, C.T. Dinh, Y. Hu, Q. Xiao, P.L. Hsieh, Y. Wang, F. Li, R. Quintero-Bermudez, Y. Zhou, P. Chen, Y. Pang, S.C. Lo, L.J. Chen, H. Tan, Z. Xu, S. Zhao, D. Sinton, E. H. Sargent, Copper-on-nitride enhances the stable electrosynthesis of multi-carbon products from  $\text{CO}_2$ , *Nat. Commun.* 9 (2018) 1–8, <https://doi.org/10.1038/s41467-018-06311-0>.
- [21] Y. Lum, J.W. Ager, Stability of residual oxides in oxide-derived copper catalysts for electrochemical  $\text{CO}_2$  reduction investigated with 18O labeling, *Angew. Chem. - Int. Ed.* 57 (2018) 551–554, <https://doi.org/10.1002/anie.201710590>.
- [22] C.W. Li, M.W. Kanan,  $\text{CO}_2$  reduction at low overpotential on Cu electrodes resulting from the reduction of thick  $\text{Cu}_2\text{O}$  films, *J. Am. Chem. Soc.* 134 (2012) 7231–7234, <https://doi.org/10.1021/ja3010978>.
- [23] Y. Hori, H. Konishi, T. Futamura, A. Murata, O. Koga, H. Sakurai, K. Oguma, “deactivation of copper electrode” in electrochemical reduction of  $\text{CO}_2$ , *Electrochim. Acta* 50 (2005) 5354–5369, <https://doi.org/10.1016/j.electacta.2005.03.015>.
- [24] I. El Baggari, B.H. Savitzky, A.S. Admasu, J. Kim, S.W. Cheong, R. Hovden, L. F. Kourkoutis, Nature and evolution of incommensurate charge order in manganites visualized with cryogenic scanning transmission electron microscopy, *Proc. Natl. Acad. Sci. U. S. A.* 115 (2018) 1445–1450, <https://doi.org/10.1073/pnas.1714901115>.
- [25] S. Zhu, X. Li, X. Jiao, W. Shao, L. Li, X. Zu, J. Hu, J. Zhu, W. Yan, C. Wang, Y. Sun, Y. Xie, Selective  $\text{CO}_2$  photoreduction into  $\text{C}_2$  product enabled by charge-polarized

metal pair sites, *Nano Lett.* 21 (2021) 2324–2331, <https://doi.org/10.1021/acs.nanolett.1c00383>.

[26] W. Luc, X. Fu, J. Shi, J.J. Lv, M. Jouny, B.H. Ko, Y. Xu, Q. Tu, X. Hu, J. Wu, Q. Yue, Y. Liu, F. Jiao, Y. Kang, Two-dimensional copper nanosheets for electrochemical reduction of carbon monoxide to acetate, *Nat. Catal.* 2 (2019) 423–430, <https://doi.org/10.1038/s41929-019-0269-8>.

[27] P. Zhu, C. Xia, C.Y. Liu, K. Jiang, G. Gao, X. Zhang, Y. Xia, Y. Lei, H.N. Alshareef, T. P. Senftle, H. Wang, Direct and continuous generation of pure acetic acid solutions via electrocatalytic carbon monoxide reduction, *Proc. Natl. Acad. Sci. U. S. A.* 118 (2021). <https://doi.org/10.1073/pnas.2010868118>.

[28] H.K. Yip, A. Schier, J. Riede, H. Schmidbaur, Benzenehexathiol as a template rim for a golden wheel: synthesis and structure of  $[\text{CSAu}(\text{PPh}_3)_6]$ , *J. Chem. Soc. Dalt. Trans.* 3 (1994) 2333–2334, <https://doi.org/10.1039/DT940002333>.

[29] X. Huang, S. Zhang, L. Liu, L. Yu, G. Chen, W. Xu, D. Zhu, Superconductivity in a Copper(II)-based coordination polymer with perfect kagomé, *Struct., Angew. Chem.* 130 (2018) 152–156, <https://doi.org/10.1002/ange.201707568>.

[30] X. Huang, Y. Qiu, Y. Wang, L. Liu, X. Wu, Y. Liang, Y. Cui, Y. Sun, Y. Zou, J. Zhu, W. Fang, J. Sun, W. Xu, D. Zhu, Highly conducting organic–inorganic hybrid copper sulfides  $\text{Cu}_x\text{C}_6\text{S}_6$  ( $x=4$  or 5.5): ligand-based oxidation-induced chemical and electronic structure modulation, *Angew. Chem.* 132 (2020) 22791–22798, <https://doi.org/10.1002/ange.202009613>.

[31] W. Wei, X. Feng, R. Wang, R. Zheng, D. Yang, H. Chen, Electrochemical driven phase segregation enabled dual-ion removal battery deionization electrode, *Nano Lett.* 21 (2021) 4830–4837, <https://doi.org/10.1021/acs.nanolett.1c01487>.

[32] B. Ravel, M. Newville, ATHENA, ARTEMIS, HEPHAESTUS: data analysis for X-ray absorption spectroscopy using IFEFFIT, *J. Synchrotron Radiat.* 12 (2005) 537–541, <https://doi.org/10.1107/S0909049505012719>.

[33] H. Xiong, H. Zou, W. Rong, Y. Wang, H. Dai, Y. Ji, L. Duan, A single-step strategy for general construction of metal sub-nanoclusters on graphdiyne, *2D Mater.* 9 (2022), <https://doi.org/10.1088/2053-1583/ac2f5f>.

[34] S.J. Clark, M.D. Segall, C.J. Pickard, P.J. Hasnip, M.I.J. Probert, K. Refson, M. C. Payne, First principles methods using CASTEP, *Z. Fur Krist.* 220 (2005) 567–570, <https://doi.org/10.1524/zkri.220.5.567.65075>.

[35] J.P. Perdew, K. Burke, M. Ernzerhof, Generalized gradient approximation made simple, *Phys. Rev. Lett.* 77 (1996) 3865–3868, <https://doi.org/10.1103/PhysRevLett.77.3865>.

[36] T.A. Halgren, W.N. Lipscomb, The synchronous-transit method for determining reaction pathways and locating molecular transition states, *Chem. Phys. Lett.* 49 (1977) 225–232, [https://doi.org/10.1016/0009-2614\(77\)80574-5](https://doi.org/10.1016/0009-2614(77)80574-5).

[37] J.K. Nørskov, J. Rossmeisl, A. Logadóttir, L. Lindqvist, J.R. Kitchin, T. Bligaard, H. Jónsson, Origin of the overpotential for oxygen reduction at a fuel-cell cathode, *J. Phys. Chem. B* 108 (2004) 17886–17892, <https://doi.org/10.1021/jp047349j>.

[38] A.A. Peterson, F. Abild-Pedersen, F. Studt, J. Rossmeisl, J.K. Nørskov, How copper catalyzes the electroreduction of carbon dioxide into hydrocarbon fuels, *Energy Environ. Sci.* 3 (2010) 1311–1315, <https://doi.org/10.1039/c0ee00071j>.

[39] W. Yang, H.J. Wang, R.R. Liu, J.W. Wang, C. Zhang, C. Li, D.C. Zhong, T.B. Lu, Tailoring crystal facets of metal–organic layers to enhance photocatalytic activity for  $\text{CO}_2$  Reduction, *Angew. Chem. - Int. Ed.* 60 (2021) 409–414, <https://doi.org/10.1002/anie.202011068>.

[40] I.D. Brown, D. Altermatt, Bond-valence parameters obtained from a systematic analysis of the Inorganic Crystal Structure Database, *Acta Crystallogr. Sect. B* 41 (1985) 244–247, <https://doi.org/10.1107/S0108768185002063>.

[41] H. Bao, Y. Qiu, X. Peng, J. ao Wang, Y. Mi, S. Zhao, X. Liu, Y. Liu, R. Cao, L. Zhuo, J. Ren, J. Sun, J. Luo, X. Sun, Isolated copper single sites for high-performance electroreduction of carbon monoxide to multicarbon products, *Nat. Commun.* 12 (2021) 1–9, <https://doi.org/10.1038/s41467-020-20336-4>.

[42] S. Kong, X. Lv, X. Wang, Z. Liu, Z. Li, B. Jia, D. Sun, C. Yang, L. Liu, A. Guan, J. Wang, G. Zheng, F. Huang, Delocalization state-induced selective bond breaking for efficient methanol electrosynthesis from  $\text{CO}_2$ , *Nat. Catal.* (2022), <https://doi.org/10.1038/s41929-022-00887-z>.

[43] B.E. Hayden, K. Kretzschmar, A.M. Bradshaw, R.G. Greenler, An infrared study of the adsorption of CO on a stepped platinum surface, *Surf. Sci.* 149 (1985) 394–406, [https://doi.org/10.1016/0039-6028\(85\)90071-8](https://doi.org/10.1016/0039-6028(85)90071-8).

[44] J. Resasco, S. Dai, G. Graham, X. Pan, P. Christopher, Combining in-situ transmission electron microscopy and infrared spectroscopy for understanding dynamic and atomic-scale features of supported metal catalysts, *J. Phys. Chem. C* 122 (2018) 25143–25157, <https://doi.org/10.1021/acs.jpcc.8b03959>.

[45] M.J. Kale, P. Christopher, Utilizing quantitative in situ FTIR spectroscopy to identify well-coordinated Pt atoms as the active site for CO oxidation on  $\text{Al}_2\text{O}_3$ -supported Pt catalysts, *ACS Catal.* 6 (2016) 5599–5609, <https://doi.org/10.1021/acscatal.6b01128>.

[46] E. Pérez-Gallent, M.C. Figueiredo, F. Calle-Vallejo, M.T.M. Koper, Spectroscopic observation of a hydrogenated CO dimer intermediate during CO reduction on Cu (100) electrodes, *Angew. Chem. - Int. Ed.* 56 (2017) 3621–3624, <https://doi.org/10.1002/anie.201700580>.

[47] S.Y. Venyaminov, F.G. Prendergast, Water ( $\text{H}_2\text{O}$  and  $\text{D}_2\text{O}$ ) molar absorptivity in the 1000–4000  $\text{cm}^{-1}$  range and quantitative infrared spectroscopy of aqueous solutions, *Anal. Biochem.* 248 (1997) 234–245, <https://doi.org/10.1006/abio.1997.2136>.

[48] N. Li, P. Yan, Y. Tang, J. Wang, X.Y. Yu, H. Bin Wu, In-situ formation of ligand-stabilized bismuth nanosheets for efficient  $\text{CO}_2$  conversion, *Appl. Catal. B Environ.* 297 (2021) 120481, <https://doi.org/10.1016/j.apcatb.2021.120481>.

[49] L. Zhang, L. Wang, H. Lin, Y. Liu, J. Ye, Y. Wen, A. Chen, L. Wang, F. Ni, Z. Zhou, S. Sun, Y. Li, B. Zhang, H. Peng, A lattice-oxygen-involved reaction pathway to boost urea oxidation, *Angew. Chem.* 131 (2019) 16976–16981, <https://doi.org/10.1002/ange.201909832>.

[50] X.F. Qiu, H.L. Zhu, J.R. Huang, P.Q. Liao, X.M. Chen, Highly selective  $\text{CO}_2$  electroreduction to  $\text{C}_2\text{H}_4$  using a metal-organic framework with dual active sites, *J. Am. Chem. Soc.* 143 (2021) 7242–7246, <https://doi.org/10.1021/jacs.1c01466>.

[51] T. Hatsukade, K.P. Kuhl, E.R. Cave, D.N. Abram, T.F. Jaramillo, Insights into the electrocatalytic reduction of  $\text{CO}_2$  on metallic silver surfaces, *Phys. Chem. Chem. Phys.* 16 (2014) 13814–13819, <https://doi.org/10.1039/c4cp00692e>.

[52] X. Zhi, Y. Jiao, Y. Zheng, S.Z. Qiao, Key to  $\text{C}_2$  production: selective C–C coupling for electrochemical  $\text{CO}_2$  reduction on copper alloy surfaces, *Chem. Commun.* 57 (2021) 9526–9529, <https://doi.org/10.1039/d1cc03796j>.

[53] Y.Y. Birdja, M.T.M. Koper, The importance of cannizzaro-type reactions during electrocatalytic reduction of carbon dioxide, *J. Am. Chem. Soc.* 139 (2017) 2030–2034, <https://doi.org/10.1021/jacs.6b12008>.

[54] T. Cheng, H. Xiao, W.A. Goddard, Full atomistic reaction mechanism with kinetics for CO reduction on Cu(100) from ab initio molecular dynamics free-energy calculations at 298 K, *Proc. Natl. Acad. Sci. U. S. A.* 114 (2017) 1795–1800, <https://doi.org/10.1073/pnas.1612106114>.

[55] H. Xiao, T. Cheng, W.A. Goddard, Atomistic mechanisms underlying selectivities in  $\text{C}_1$  and  $\text{C}_2$  products from electrochemical reduction of CO on Cu(111), *J. Am. Chem. Soc.* 139 (2017) 130–136, <https://doi.org/10.1021/jacs.6b06846>.

[56] F. Calle-Vallejo, M.T.M. Koper, Theoretical considerations on the electroreduction of CO to  $\text{C}_2$  species on Cu(100) electrodes, *Angew. Chem.* 125 (2013) 7423–7426, <https://doi.org/10.1002/ange.201301470>.

[57] H. Bai, T. Cheng, S. Li, Z. Zhou, H. Yang, J. Li, M. Xie, J. Ye, Y. Ji, Y. Li, Z. Zhou, S. Sun, B. Zhang, H. Peng, Controllable CO adsorption determines ethylene and methane productions from  $\text{CO}_2$  electroreduction, *Sci. Bull.* 66 (2021) 62–68, <https://doi.org/10.1016/j.scib.2020.06.023>.

[58] H. Xiao, W.A. Goddard, T. Cheng, Y. Liu, Cu metal embedded in oxidized matrix catalyst to promote  $\text{CO}_2$  activation and CO dimerization for electrochemical reduction of  $\text{CO}_2$ , *Proc. Natl. Acad. Sci. U. S. A.* 114 (2017) 6685–6688, <https://doi.org/10.1073/pnas.1702405114>.